Journal of Magnetism and Magnetic Materials 465 (2018) 747–755

Contents lists available at ScienceDirect

Journal of Magnetism and Magnetic Materials

journal homepage: www.elsevier.com/locate/jmmm

Research articles

Influence of iron content on the structural and magnetic properties of Ni-Zn ferrite nanoparticles synthesized by PEG assisted sol-gel method

P.V. Ramana[a], K. Srinivasa Rao[b,*], K.H. Rao[c]

[a] Department of Physics, A.G & S.G Siddhartha Degree College of Arts and Science, Vuyyuru 521165, India
[b] Department of Physics, P.B.N. College, Nidubrolu 522 124, India
[c] IIIT, RGUKT, Nuzvid 521202, India

ARTICLE INFO

Keywords:
Ni-Zn ferrite
Sol-gel process
Magnetic properties
TEM & FESEM images

ABSTRACT

Ni-Zn ferrite nanoparticles of smaller particle size and high saturation magnetization have gained a special attention for their use in biomedical applications. The development of such nanoparticles requires rigorous processing conditions in arriving at desired characteristics. Ni-Zn ferrite nanoparticles of three different compositions $Ni_{0.65}Zn_{0.35}Fe_2O_4$, $Ni_{0.65}Zn_{0.40}Fe_{1.95}O_4$ and $Ni_{0.60}Zn_{0.35}Fe_{2.05}O_4$ containing varying amounts of iron concentration 50.00 mol%, 48.75 mol%, and 51.25 mol% respectively were processed by the sol-gel method using polyethylene glycol (PEG) as a chelating agent and characterized by techniques X-ray diffraction, Transmission electron microscopy, field emission scanning electron microscopy and Fourier transform infrared spectroscopy in elucidating the structural parameters. Ferrite compositions containing lower and higher iron content require the lower annealing temperature to produce higher saturation magnetization as compared to the stoichiometric composition. The composition of lower iron content favoured smaller particle size of 9 nm, while the material of higher iron content showed enhanced saturation magnetization of 91.9 emu/g. From the knowledge of literature and our previous works, it is opined that no other chelating agent than PEG proved to be an efficient one in controlling the particle size and improving the microstructure.

1. Introduction

Ni-Zn ferrites have been the subject of investigation for the past several years due to their exciting and growing industry applications. The extensive study of several researchers on Ni-Zn ferrite system has revealed that Ni-Zn bulk ferrite is the only core material useful for high frequency applications due to its reasonably high saturation magnetization, moderate magnetic permeability, high Curie temperature, moderate DC resistivity and low power loss [1,2]. The properties of bulk ferrites are highly sensitive to the method of processing, the amount of constituent ions and the kind of impurities present in the system [3]. The high sintering temperatures adopted in conventional ceramic technique are, in general, promote undesirable aspects like the evaporation of zinc from the product, formation of larger grains, presence of impurity secondary phases, and ferrous ions [4,5]. In circumventing these, most of the researchers had introduced sintering aids [6–8] for the preparation of Ni-Zn ferrites at lower temperatures. However, the formed bulk products have shown no significant changes in their properties. The usage of bulk nickel-zinc ferrites as core material is limited to 100 MHz due to their moderate saturation magnetization and DC resistivity. The operational frequency of core material beyond 100 MHz can be made possible by increasing the specific saturation magnetization and the DC resistivity of the ferrite for which the material is to be processed in nano form [1,9].

In recent years, nanosized ferrites have been extensively investigated by several researchers to overcome the drawbacks associated with the bulk ferrites [10,11]. Nanomaterials exhibit spectacular, exotic, and useful properties for various applications when material length scale is comparable to property length scale [12]. Among the magnetic properties, the saturation magnetization, initial permeability, coercivity and remnant magnetization were found to vary greatly with the particle size [13]. The nanosized material has the advantage of being synthesized at relatively low temperatures for a short duration, which not only saves time, cost, and power consumption, but also prevents evaporation of zinc. Nowadays, Ni-Zn nanoferrites play a crucial role due to their wide range of potential applications such as MRI contrast enhancing agents, magnetic carriers for drug targeting, magnetic fluids, high density information storage devices and multilayer chip inductors [14,15]. These potential applications solely depend on the characteristics of the product such as least particle size, high

* Corresponding author.
E-mail address: ksr_gvsk@yahoo.co.in (K. Srinivasa Rao).

https://doi.org/10.1016/j.jmmm.2018.06.065
Received 20 April 2018; Received in revised form 14 June 2018; Accepted 21 June 2018
Available online 22 June 2018
0304-8853/

saturation magnetization, low coercive force and single domain nature.

In bulk Ni-Zn mixed ferrite with general formula AB_2O_4, tetrahedral sites are occupied by Zn^{2+} and Fe^{3+} ions, while octahedral sites accommodate Ni^{2+} and Fe^{3+} ions. The electrical and magnetic properties of the ferrite are decided by the kind and amounts of various cations present in the composition. Hua Su et al. [16] reported that a slight deficiency or excess of Fe_2O_3 content as compared to that of stoichiometric nickel-zinc ferrite had no pronounced influence on saturation magnetization, while a slight excess of Fe_2O_3 showed an effective improvement in initial permeability. Ling et al. [17] investigated the effects of iron deficiency on the frequency spectra and temperature stability of permeability by controlling the amount of iron in Ni-Zn ferrites. Sun et al. [18] studied the effects of iron-deficient, stoichiometric and iron-excessive compositions on the phase formation, crystal structure, grain growth and magnetic properties of NiCuZn ferrites. The grain size, density, saturation induction and initial permeability have been reported to increase initially and followed by a decrease as the Fe_2O_3 amount present in the system changes from 47 mol% (iron deficiency) to 54 mol% (iron excess). Xinhua He et al. [19] synthesized non-stoichiometric Ni-Zn ferrites by a sol-gel method and studied the influence of annealing temperature as well as the amount of Fe deficiency on phase evolution, crystal structure and crystallite size of spinel ferrites.

Although the iron content present in a composition is known to affect the structural and electromagnetic properties considerably, the investigations conducted, so far, either in bulk or nano Ni-Zn ferrites containing varying amounts of iron content are extremely inadequate. Moreover, the existing information in the literature is insufficient in providing a clear and rigid picture about the influence of iron content on saturation magnetization in a ferrite composition.

Ni-Zn ferrite nanoparticles were synthesized by several researchers adopting different methods in understanding the particle size related magnetic properties [20,21]. Gao et al. [22] produced $Ni_{1-x}Zn_xFe_2O_4$ (x = 0.0, 0.5 and 1.0) nanoparticles by sol gel method with grain size in the range 29 nm to 40 nm and observed the critical size for single domain particles of $Ni_{0.5}Zn_{0.5}Fe_2O_4$ around 24 nm with saturation magnetization 53 emu/g. Caizer et al. [23] processed $Ni_{0.35}Zn_{0.65}Fe_2O_4$ nanoparticles of size ranging from 20 nm to 38 nm by a new chemical method (hetero-poly nuclear complex combination) and arrived at the critical size of single domain particle around 29 nm with saturation magnetization less than 40 emu/g. An attempt was made by A.M. Kumar et al. [1] in achieving high saturation magnetization of 80 emu/g in $Ni_{0.65}Zn_{0.35}Fe_2O_4$ ferrite nanoparticles of crystallite size 42 nm prepared by the sol-gel method. For magnetic heating applications, in general, the size of the required particles, exhibiting single domain superparamgnetic nature is usually less than 10 nm with possible high saturation magnetization in the range 70 emu/g to 80 emu/g [24].

The growth mechanism of the particles, at higher annealing temperatures above 600 °C, takes place through coalescing and agglomeration [25–27]. To prevent agglomeration and control the particle size adequately, generally surfactant or chelating agents are employed during synthesizing the ferrite nanoparticles. Efforts have been made by several research groups [28,29] to achieve a fine tuning of the size of the nanoparticles, employing different surfactants and chelating agents. The reports available in the literature mainly focus on the synthesis of magnetic nanoparticles using PEG as surfactant to prevent agglomeration and to obtain smaller particle sizes with good crystallinity [30,31].

Zhang et al. [32] synthesized Mn-Zn ferrite nanoparticles in the range 35 nm to 25 nm by a direct chemical coprecipitation and refluxing process using PEG6000 as surfactant and observed high saturation magnetization of 110 emu/g in particles of size 25 nm. Köseoğlu et al. [33] developed superparamagnetic $Mn_{0.2}Ni_{0.8}Fe_2O_4$ nanoparticles of size 6.5 nm by PEG assisted hydrothermal method with saturation magnetization 32 emu/g. Kavas et al. [34] reported the synthesis of $Ni_{1-x}Zn_xFe_2O_4$ (x = 0.0 to 1.0 in steps of 0.2) nanoparticles in the range 20 nm to 9 nm by hydrothermal method using polyethylene glycol as a surfactant with superparamagnetic nature at room temperature. An attempt was made by M. Sertkol et al. [30] in producing superparamagnetic $Zn_{0.6}Ni_{0.4}Fe_2O_4$ ferrite nanoparticles of size 15 nm with saturation magnetization 40.3 emu/g by hydrothermal method using PEG as surfactant.

Although polyethylene glycol has played an important role as surfactant to prevent agglomeration and in controlling particle size, the particle size in most of the cases has been observed to be more than 10 nm. The kind of chelating agent and its proportionate amount present in the precursor are responsible in obtaining the nanoparticles with controlled particle size through a careful heat treatment. In our recent reports, the influence of chelating agent, polyvinyl alcohol in yielding fine particles of the required size with high saturation magnetization was dealt with in detail [35]. From the knowledge of our previous work, the rise in saturation magnetization may further be envisaged for fine particles of smaller size using PEG as chelating agent.

In the present work, the familiar Ni-Zn composition $Ni_{0.65}Zn_{0.35}Fe_2O_4$ (named IN) with two other close compositions $Ni_{0.65}Zn_{0.35}Fe_{2.05}O_4$ (named IE), and $Ni_{0.65}Zn_{0.4}Fe_{1.95}O_4$ (named ID) have been chosen and processed by the sol-gel method using polyethylene glycol as chelating agent. The results obtained from various techniques related to microstructure, magnetic properties, and cation distribution of Ni-Zn ferrite nanoparticles corresponding to IN, ID and IE compositions have been discussed in detail in relation to the heat treatment.

2. Experimental details

2.1. Method of preparation

Analytical reagent grade iron, nickel and zinc nitrates were used as ingredients in the preparation of $Ni_{0.65}Zn_{0.35}Fe_2O_4$ (IN), $Ni_{0.65}Zn_{0.40}Fe_{1.95}O_4$ (ID) and $Ni_{0.60}Zn_{0.35}Fe_{2.05}O_4$ (IE) ferrite particles by sol-gel method using PEG as a chelating agent, keeping the ratio of ferrite to PEG by weight at 1:1. Adopting the method of preparation, as described in an earlier paper [35], the dried (as-prepared) ferrite powders were annealed at 400 °C in the air for one hour before subjecting the materials to natural cooling. The annealed powder of each sample was crushed thoroughly and pressed into pellets and toroids using polyvinyl alcohol as a binder for further heat treatment in air for 1 more hour at different temperatures 800 °C, 900 °C, 1000 °C and 1050 °C with a heating rate of 5 °C/minute. The optimum annealing/sintering temperature has been fixed based on specific saturation magnetization measurement.

2.2. Characterization

The formation of spinel structure of all the annealed samples was investigated with X-ray Bruker advanced D8 X-ray diffractometer, employing Cu-K_α radiation (λ = 1.5406 Å). In determining the particle size, Transmission Electron Micrographs were obtained from JOEL JEM 200CX model electron microscope operated at the electron accelerating voltage of 120 kV. The room temperature infrared spectrum of each sample was recorded using the FTIR spectrometer (Perkin Elmer model 1650) in the range of 300–4000 cm^{-1} by KBr pellet method. Specific saturation magnetization at room temperature was recorded with the help of vibrating sample magnetometer (Lake Shore 4700) by applying a maximum field of 18 kOe. The temperature dependence of magnetic permeability of all the samples was measured using 6500P WAYNE KERR high frequency LCR meter. The experimental density, obtained for each sample from the Archimedes' principle was compared with that of theoretical, obtained from the equation $d_x = 8\,M/Na^3$, where M is the molecular weight of the composition, N is the Avogadro's number and 'a' is the lattice parameter.

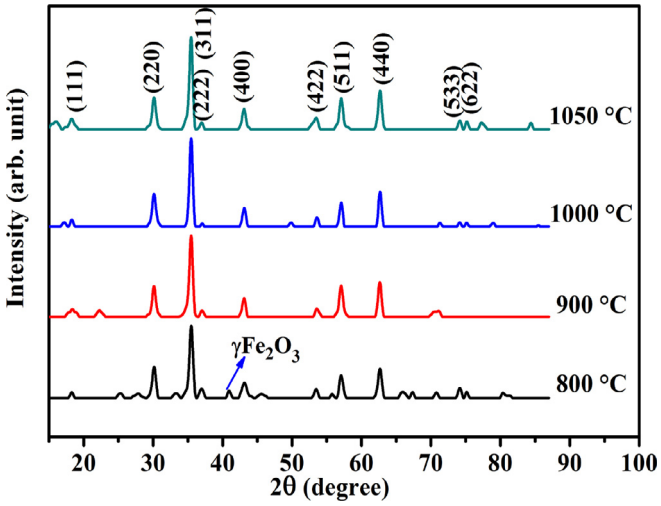

Fig. 1. X-ray diffraction patterns of IN sample heated at different temperatures.

3. Results and discussion

3.1. X-ray diffraction

Figs. 1–3 show X-ray diffraction patterns of IN, ID and IE, Ni-Zn nanoferrite powders annealed at temperatures ranging from 800 °C to 1050 °C. The presence of iron oxide phase at lower annealing temperature 800 °C appears to impede the formation of pure Ni-Zn ferrite due to slower atomic diffusion. The single-phase spinel structure was confirmed in all the samples, annealed above 800 °C.

The considerable amount of line broadening present in all the diffraction peaks of the samples suggests that the size of the crystallite is expected to be relatively small. The observed gradual increase in both sharpness and intensity of peaks asserts the improved crystallization process with temperature.

The crystallite size has been estimated from Williamson-Hall plots using the equation for the size and strain broadenings [36]

$$\frac{\beta\cos\theta}{\lambda} = \frac{1}{D} + \frac{4\varepsilon\sin\theta}{\lambda} \quad (1)$$

where $\beta = \sqrt{(\beta^2_{Measured} - \beta^2_{Instrumental})}$ is the peak broadening after removing the instrumental broadening, λ (1.5406 Å) is the wavelength of X-rays used and θ is the peak center. A graph drawn between $\frac{\beta\cos\theta}{\lambda}$ versus $\frac{4\sin\theta}{\lambda}$ is a straight line and the reciprocal of the intercept along y-axis at $\sin\theta = 0$ gives the crystallite size. Thus, the estimated crystallite size (Fig. 4) has been found to vary from 10 to 12 nm for IN, 7 to 11 nm for ID and 9 to 13 nm in case of IE samples respectively. A gradual rise in crystallite size has been observed with increasing firing temperature up to 1050 °C for IN sample. On the other hand, a gradual increase up to 1000 °C, followed by rapid increase for further rise in temperature has been observed in both IE and ID samples. The observed changes have been attributed to increase in thermal energy which favors elimination of defects, relieving internal stresses and activity of the crystallization process. Similar findings were reported earlier [35] in respect of crystallite and particle size variation as a function of annealing temperatures.

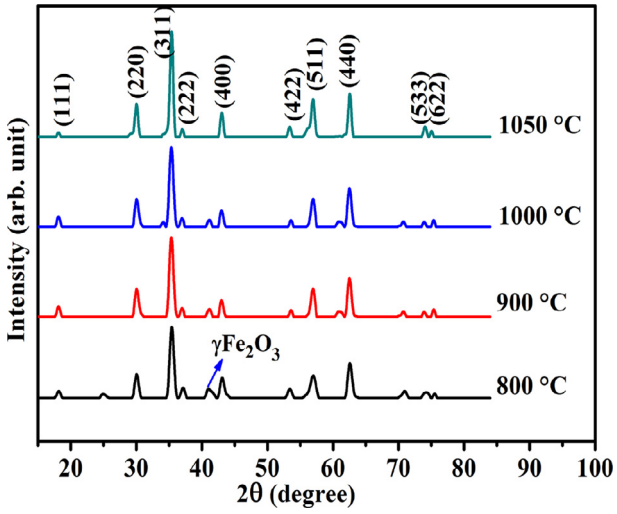

Fig. 2. X-ray diffraction patterns of ID sample heated at different temperatures.

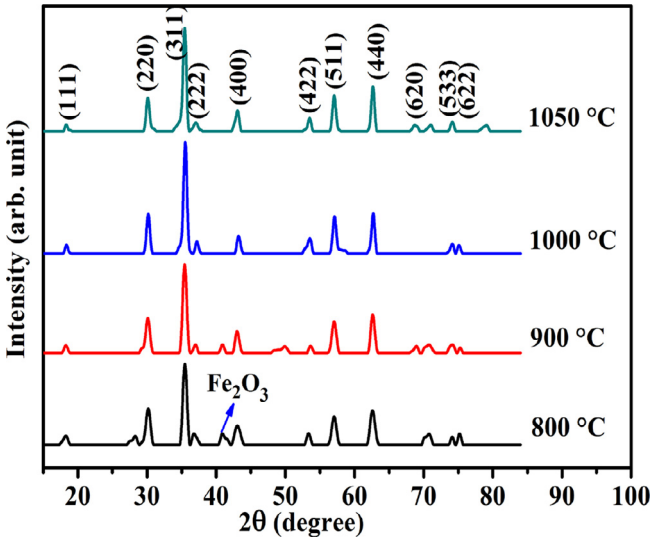

Fig. 3. X-ray diffraction patterns of IE sample heated at different temperatures.

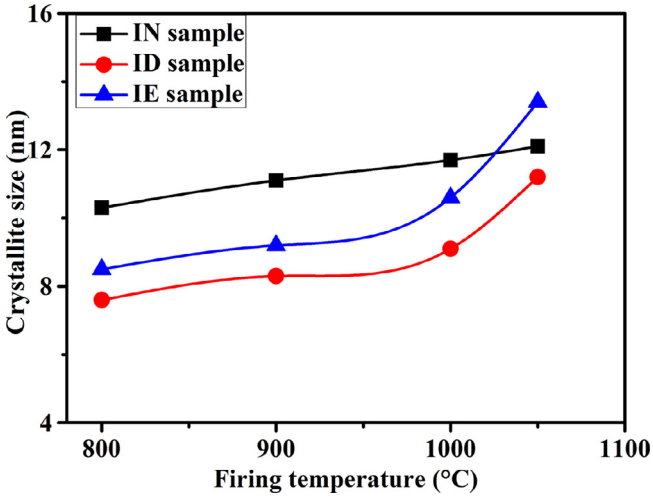

Fig. 4. Variation of crystallite size with firing temperature.

During annealing the dried powder to 400 °C, PEG residue causes a reduction in particle to particle distance during its decomposition process. Annealing at higher temperatures promotes crystallization and increases the surface energy leading to the coalescence among the particles by sharing common grain boundaries in the sample. The growth in crystallite size beyond annealing temperature 1000 °C in case of both ID and IE samples might be due to the sintering mechanism where the surface free energy of particle decreases because of the contributions arising from solid-vapor (particle-pore) interface energy and solid-solid interface energy [37]. During the sintering process, the decrease in solid-vapor interface energy is more than the increase in

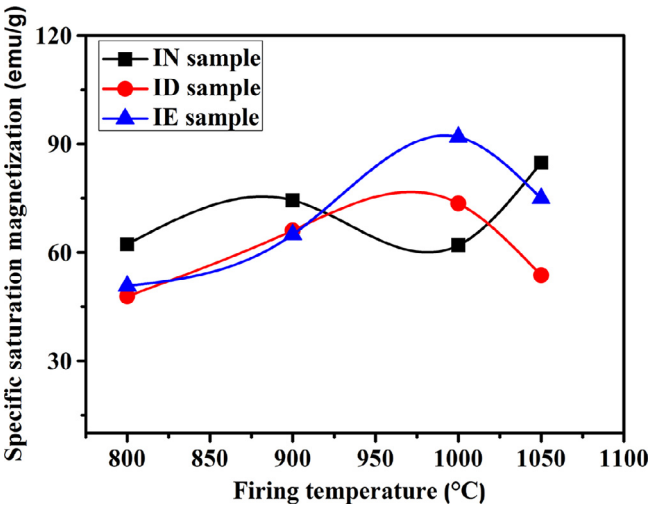

Fig. 5. Variation of specific saturation magnetization with firing temperature.

solid-solid interface energy. Thus, the firing temperature above 1000 °C initiates the grain growth by combining the grains and reduces the total surface energy of the IE and ID systems.

The selection of optimum firing temperature of the samples has been made based on specific saturation magnetization measurement at room temperature as a function of annealing temperature, Fig. 5. The graph shows high magnetization at 1000 °C in ID and IE samples, while at 1050 °C in the IN sample. Accordingly, the temperatures 1000 °C for ID and IE and 1050 °C for IN have been the optimum annealing temperatures employed for processing and the samples are designated as ID-1000 and IE-1000 and IN-1050. Further, the work presented in the following pages is confined to these three ID-1000, IE-1000 and IN-1050 samples only.

Lattice parameter for IN-1050, ID-1000, and IE-1000 samples has been estimated from the observed Bragg angles of X-ray diffraction pattern considering Nelson-Riley function to minimize the error in its determination. The lattice parameter for IN sample has been observed to be in good agreement with that reported [38].

The bulk density, determined using the Archimedes' principle for the three samples, is given in Table 1 along with crystallite size, particle size and porosity. The observed higher bulk density of IE-1000 as compared to the other two samples may be due to the generation of Fe^{2+} ions at higher annealing temperature. The observed slight increase in lattice parameter in case of IE-1000 also supports the formation of Fe^{2+} ions in the material. The increased lattice constant is due to higher ionic radius (0.78 Å) of the Fe^{2+} ions than that of Fe^{3+} ions (0.645 Å). At higher sintering temperatures, reduction of Fe^{3+} ions into Fe^{2+} ions and thereby creation of oxygen vacancies results in high density with larger grains [39]. FESEM micrographs of these three samples support the observed microstructural changes in terms of increased porosity and compaction of reduced grains (Fig. 6).

Table 1
Lattice parameter, crystallite size, particle size, bulk density, X-ray density and percentage of porosity of nanosized Ni-Zn ferrite samples.

Sample	Lattice parameter (Å)	Crystallite size (nm)	Particle size (TEM) (nm0029	Bulk density (g/cm^3)	X-ray density (g/cm^3)	Percentage of porosity
IN-1050	8.3746	12	12.8	4.498	5.355	16.0
ID-1000	8.3774	9	9.0	4.516	5.360	15.8
IE-1000	8.3806	10	10.8	4.577	5.340	14.3

3.2. Transmission electron micrographs

Transmission Electron Micrographs, histograms and SAED patterns of three Ni-Zn ferrite samples, IN-1050, ID-1000 and IE-1000 are shown in Fig. 7. Mean particle size has been estimated from a transmission electron micrograph considering the observed linear size of the particles at different locations using Image J software by fitting the particle size distribution with a Gaussian function. The particle size estimation involves a count of about 120 particles taken from two image pictures of each sample. The images reflect the agglomerated characteristic of the prepared nanoparticles to a certain extent, where the primary particles are held together.

The estimated average particle size lies in the range of 9.0 to 12.8 nm and agrees well with the crystallite size obtained from X-ray diffraction patterns. Thus, the adopted sol-gel method is assured of providing smaller crystallite and particle sizes at optimum annealing temperature. The particle size reduction in the sample ID-1000 has been ascribed to the reduced number of Fe^{2+} ions at optimum sintering temperature and the presence of Fe^{2+} ions has also been confirmed through FTIR spectra, discussed in the next section.

3.3. Fourier transform infrared spectra

The room temperature FTIR spectra of IN-1050, IE-1000 and ID-1000 samples are shown in Fig. 8.

The observed absorption bands for Ni-Zn ferrite powder in the range (592–595 cm^{-1}) and (414–420 cm^{-1}) have been attributed to the vibrations of $Fe^{3+} \leftrightarrow O^{2-}$ at tetrahedral and octahedral sites respectively [40]. The absorption band 2360 cm^{-1} has been assigned to the atmospheric carbon dioxide adsorbed on the surface of the particles during the preparation of the samples [41]. A weak band observed at around 470 cm^{-1}, ascribed to the splitting of the octahedral band due to the Jahn-Teller distortion, confirms the presence of Fe^{2+} - O^{2-} vibration band in the ferrite [42]. The band positions correspond to tetrahedral and octahedral metal complexes are presented in Table 2.

The tetrahedral band (υ_1) of ID-1000 and octahedral band (υ_2) of IE-1000 show a shift towards the higher wave numbers with respect to the corresponding bands of IN-1050. The tetrahedral band shift indicates that Zn^{2+} (0.60 Å) ions prefer to occupy tetrahedral sites and push Fe^{3+} ions towards oxygen ions by which the distance between Fe^{3+} - O^{2-} ions is expected to decrease due to larger ionic radius of Zn^{2+} than Fe^{3+} (0.49 Å) ion. The existence of a weak absorption band, 668 cm^{-1} could be attributed to the presence of the Zn^{2+} ions at the tetrahedral sites [43] corresponding to the Zn^{2+} - O^{2-} tetrahedral complexes. The band intensity has shown an increase with the zinc concentration (Fig. 9) in the ID-1000 sample.

The shift of the octahedral absorption band in the IE-1000 sample is due to change in bond length at B-sites, causing an increase in force constant of the octahedral site in comparison with the normal sample. The force constant for the bond Fe^{3+} - O^{2-} has been calculated using the equation [44]

$$K = 4\pi^2 c^2 \nu^2 \mu \quad (2)$$

(all values are in CGS), where c is the speed of light, ν is the wave number and μ is the reduced mass for Fe^{3+} and O^{2-} ions. The estimated force constants for the tetrahedral and octahedral sites are given in Table 2. In general, the decrease in bond length, and increase in force constant for either site may be expected if the radius of the impurity ion is smaller than the displaced ion. In the IE-1000 sample, the displaced nickel ion concentration is same as the excess iron ion concentration. The increase in iron concentration at octahedral sites could improve the reduced mass, besides the displacing the nickel ions at octahedral sites and the process is responsible for the observed variation in band position and force constant.

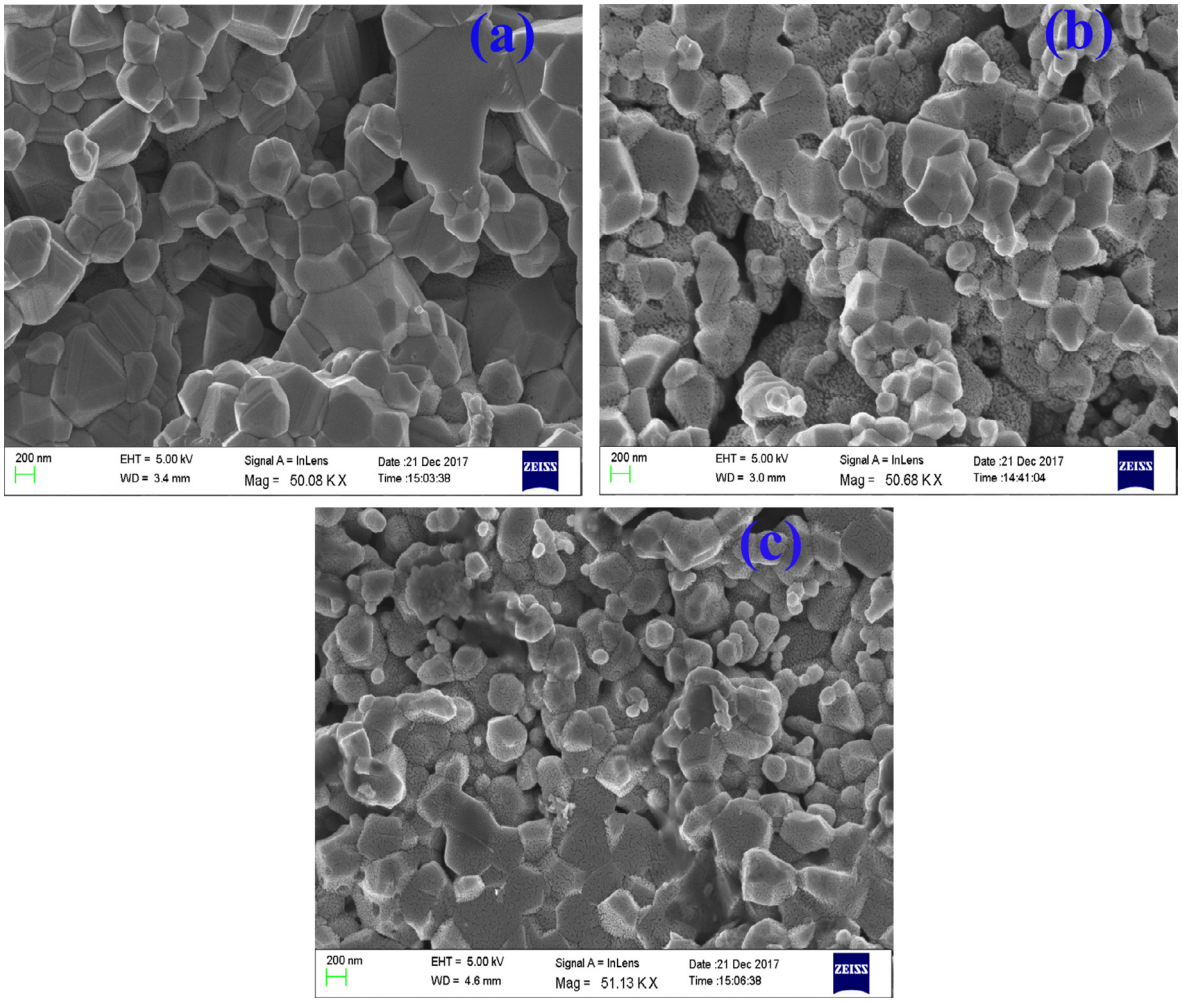

Fig. 6. FESEM images of (a) IN-1050 ,(b) ID-1000 and (c) IE-1000 pellet samples.

3.4. Magnetic properties

Room temperature hysteresis loops for IN-1050, ID-1000 and IE-1000 samples in an applied magnetic field of 20 kOe are shown in Fig. 10. To know the value of coercive field clearly, the origin portion has been magnified and given inset. All the samples have been observed to exhibit room temperature hysteresis under the applied magnetic field.

The specific saturation magnetization and coercivity parameters, derived from magnetic loops are presented in Table 3.

The observed specific saturation magnetization values, in the present investigation are higher than those reported by other researchers in Ni-Zn nanoferrite systems, synthesized by different methods [20,34,45]. IE-1000 sample with particle size 10.8 nm has been observed to yield the highest specific saturation magnetization of 91.9 emu/g which is higher than that reported for the same composition [46]. Further, the values of saturation magnetization are shown to be greater than those observed in bulk ferrites of near composition [38,1]. It is noted that the PEG assisted sol-gel method has the capability of yielding the ferrite material of higher specific saturation magnetization processed at a relatively lower sintering temperature for shorter duration in contrast to the ceramic method.

The variation in saturation magnetization can be understood based on exchange interactions between ions present at tetrahedral and octahedral sites in the spinel lattice. According to Neel model, A-B exchange interaction in ferrites is stronger and effective than A-A and B-B super exchange interactions and the net magnetic moment of the ferrite lattice is equal to the difference between the magnetic moments of A and B sublattices, i.e. $M = M_B - M_A$ [47]. The exchange interactions in the spinel lattice can greatly be influenced by the nature of the ions present at both A and B sublattices. Ni-Zn ferrite is a mixed spinel in which all Zn^{2+} ions occupy tetrahedral (A) sites, Ni^{2+} ions occupy octahedral (B) sites and Fe^{3+} ions are distributed between tetrahedral and octahedral sites.

In the IE-1000 sample, nickel concentration decreases by 1.25 mol% against an increase in iron concentration by the same amount. This kind of substitution causes an increase in the magnetic moment of the B-sites as the magnetic moment of Fe^{3+} ($5\mu_B$) ion is greater than the Ni^{2+} ($2\ \mu_B$) ion, by $3\ \mu_B$ and thereby leading to the higher magnetization of the IE-1000 sample with respect to the IN-1050 sample. In the present study, the observed lower saturation magnetization for ID-1000 sample could be because of the decrease in particle size as compared to the other two samples. The decrease in particle size favors number of atoms on its surface due to large surface to volume ratio. Because of the canted spins at the surface (shell) of the nanoparticles, no true saturation is possible even at very high applied magnetic field in accordance with the core-shell model of the nanoparticles [48,49]. The observed changes can further be supported considering the effects of magneto-crystalline anisotropy constant and Curie temperature of the samples.

The magneto-crystalline anisotropy constant (K) has been obtained using the relation [44],

$$K = \frac{M_S \times H_C}{0.96} \quad (3)$$

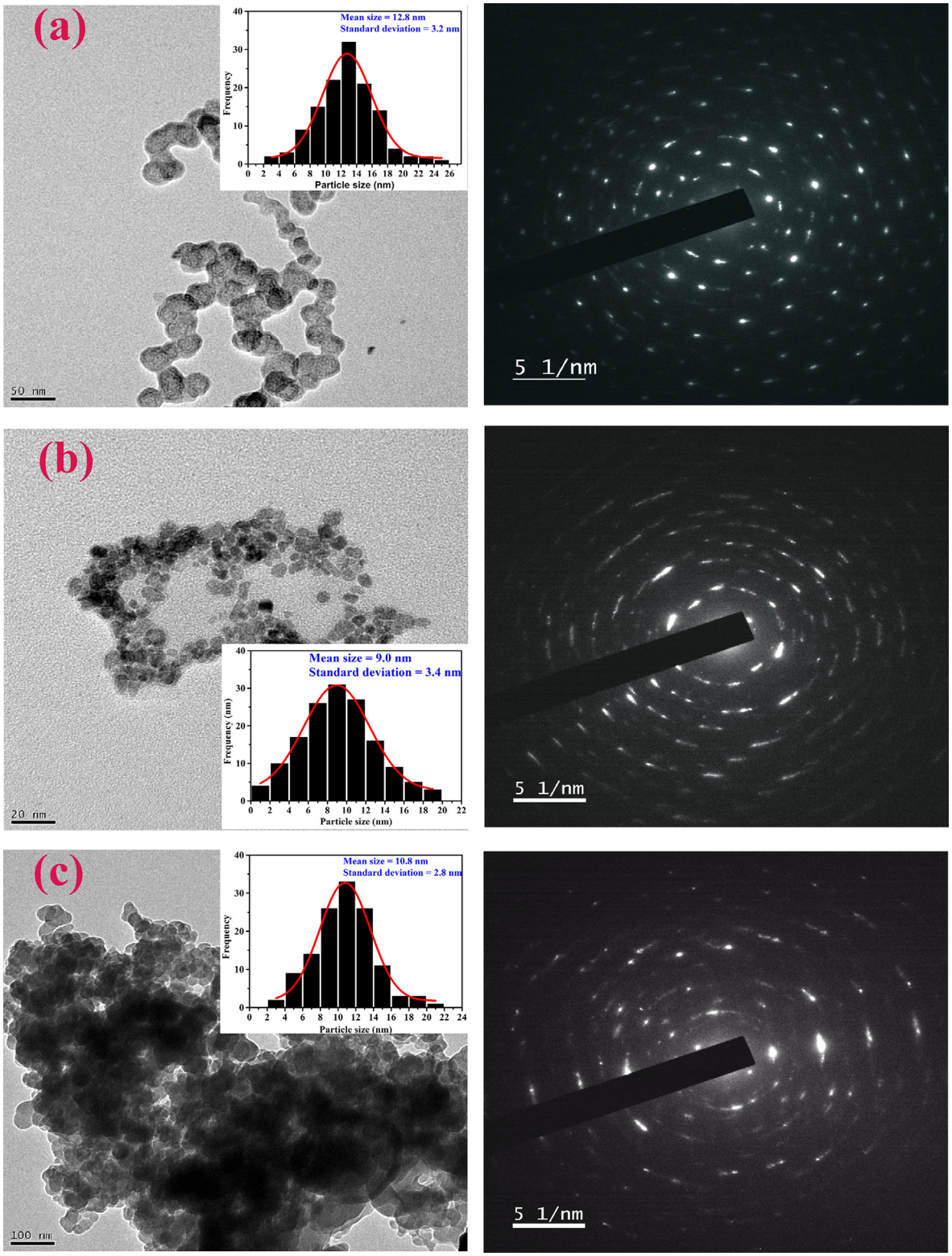

Fig. 7. TEM images, Histograms and SAED patterns of (a) IN-1050. (b) ID-1000 and (c) IE-1000 powder samples.

where H_c is coercive field in Oe, Ms. is the maximum value of magnetization measured at 18 kOe applied magnetic field and the values are shown in Table 3. Among the three samples, the highest magnetic anisotropy constant (3.53×10^5erg/cm^3) has been associated with IE-1000. As is known, the magnetic anisotropy in non-cobalt containing ferrites arises from the Fe^{3+} ions present at the B-sub lattices. Several researchers reported that the anisotropy of the ferrites depends on the formation of highly anisotropic Fe^{2+} ions (stronger spin-orbit coupling) in the system [50,51]. Thus, in the present work, the increase in the magneto-crystalline anisotropy constant with iron concentration may be expected due to the formation of more number of Fe^{2+} ions, which is reflected in the observed increase in coercivity of the samples.

The Curie temperature, measured from the temperature dependence of initial permeability (μ_i) in the range 40 – 450 °C for three samples at a

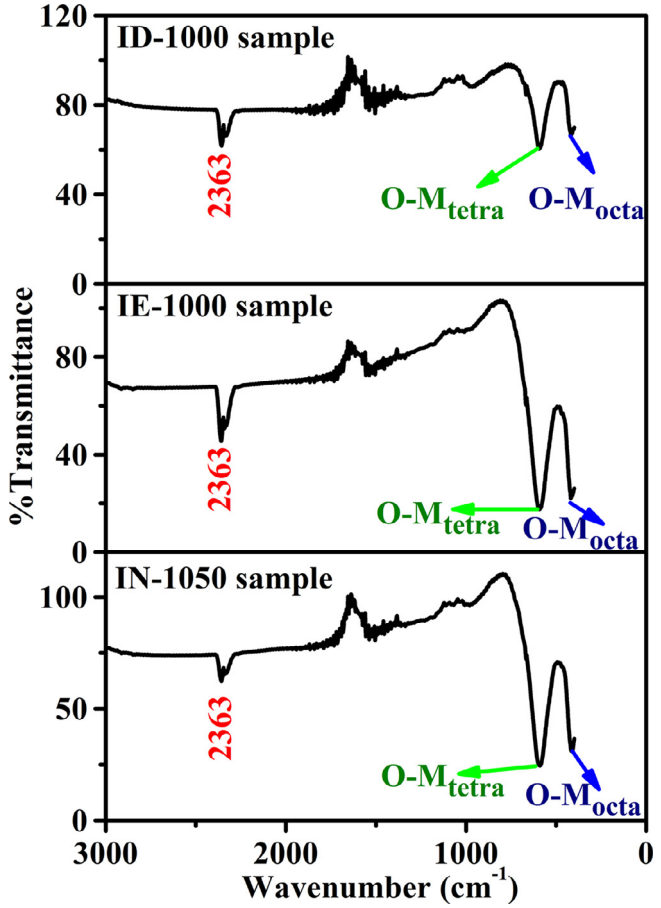

Fig. 8. FTIR spectra of Ni-Zn ferrites.

Table 2
Band positions and Fe^{3+}–O^{2-} bond force constants for Ni-Zn ferrites.

Sample	ν_1 (tetrahedral) (cm^{-1})	ν_2 (octahedral) (cm^{-1})	Fe^{3+}–O^{2-} bond force constant (10^5 dyne/cm)	
			Tetrahedral (K_T)	Octahedral (K_O)
IN-1050	592	414	2.27	1.33
ID-1000	595	417	2.23	1.35
IE-1000	593	420	2.28	1.37

constant frequency 100 kHz is shown in Fig. 11. An abrupt drop in initial permeability near the Curie point indicates a good compositional homogeneity. The absence of secondary maximum in μ_i versus T graph indicates the formation of single phase ferrite samples as shown by XRD

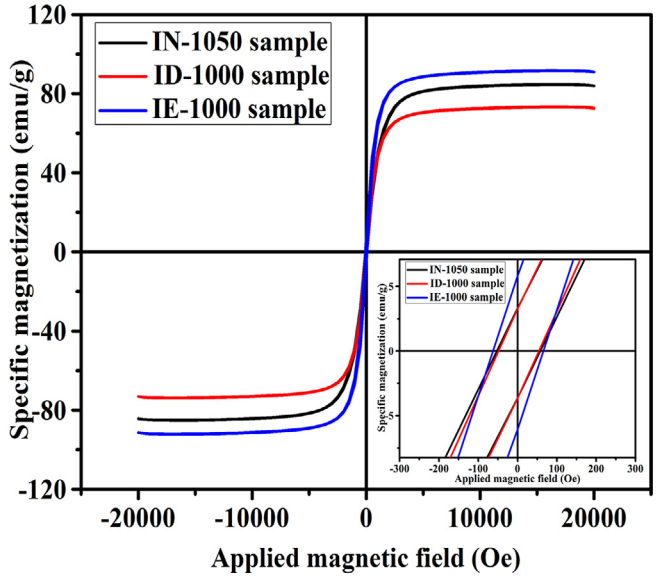

Fig. 10. Room temperature hysteresis loops of Ni-Zn ferrites.

Table 3
Saturation magnetization, Coercivity, Anisotropy constant and Curie temperature of nanosized Ni-Zn ferrite samples.

Sample	Specific saturation magnetization (emu/g)	Coercivity (Oe)	Anisotropy constant (10^5 erg/cm^3)	Curie temperature (°C)
IN-1050	84.9	55.3	2.76	408
ID-1000	73.4	51.4	2.24	297
IE-1000	91.9	64.1	3.53	360

patterns.

The Curie temperature values (Table 3) for the Ni-Zn ferrites have been found to be higher than those reported for the nearer compositions, prepared under different methods [40,52,53]. Based on the observation, it may be inferred that some stronger interactions might be prevailing besides the strongest A-B exchange interactions between the nanoparticles, which would lead to the noticed higher values of saturation magnetization as well as high Curie temperature.

The lower Curie temperature of ID-1000 sample is attributed to the lower particle size and zinc concentration in the composition. As the net magnetic moment of the lattice is the difference between the magnetic moments of the B and A sublattices, it is obvious that the exchange interactions among the ions would increase with both the density of magnetic ions and their magnetic moments. The increase in diamagnetic zinc content in the ID-1000 sample reduces the magnetic moment of the A-sublattice and weakens the A-B exchange interaction, resulting in lower Curie temperature of the ID-1000 sample as compared with

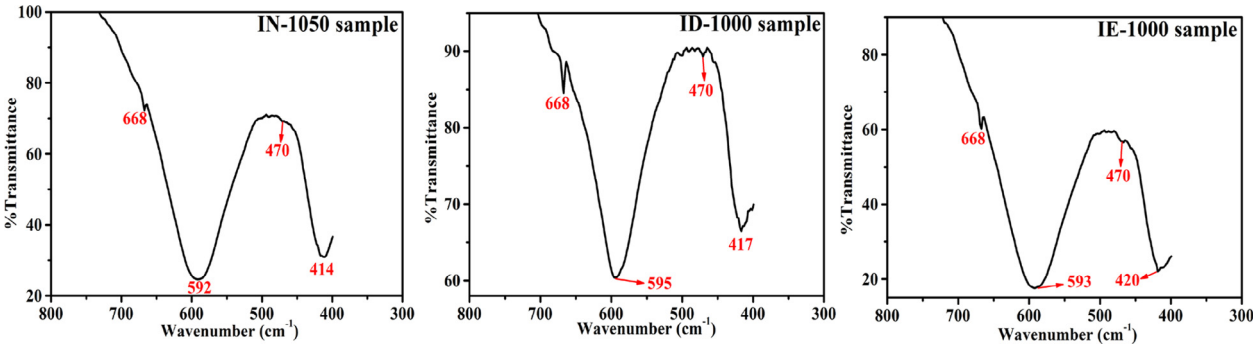

Fig. 9. Magnified pictures of absorption bands of Ni-Zn ferrites.

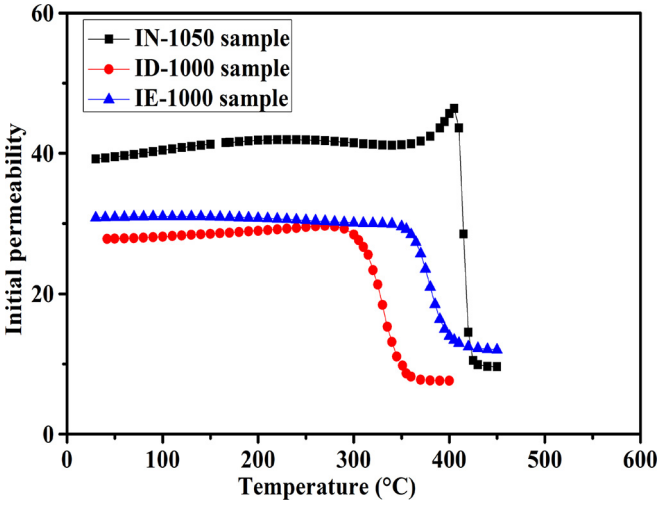

Fig. 11. Variation of initial permeability with temperature in Ni-Zn ferrites.

Table 4
Proposed cationic distribution, calculated lattice parameter, oxygen parameter and bond lengths of Ni-Zn ferrite samples.

Sample	Proposed cation distribution	Calculated lattice parameter (Å)	u	Bond length (Å)	
				Tetrahedral (d_{AO})	Octahedral (d_{BO})
IN-1050	$(Zn_{0.35}\ Fe_{0.65})$ $[Ni_{0.65}\ Fe_{1.35}]$ O_4	8.3772	0.382	1.909	2.041
ID-1000	$(Zn_{0.40}Fe_{0.60})$ $[Ni_{0.65}Fe_{1.35}]$ O_4	8.3856	0.382	1.914	2.041
IE-1000	$(Zn_{0.35}Fe_{0.65})$ $[Ni_{0.60}\ Fe_{1.40}]$ O_4	8.3806	0.382	1.904	2.040

other two samples.

3.5. Cation distribution

Based on the preferences of various metallic ions discussed above, the cation distribution for the series of samples has been proposed. Further, to check the correctness of the proposed distributions, lattice constant (a) has been calculated for each composition using the proposed distribution and some needy mathematical formulae as given below [47];

$$a_{Calculated} = \frac{8}{3\sqrt{3}}[(r_A + R_0) + \sqrt{3}(r_B + R_0)] \quad (4)$$

where r_A and r_B are the mean radii of the tetrahedral and octahedral sites and R_o is the radius of oxygen ion (1.38 Å). Shanon radii (radii of cations in respective sites) [40] have been used in determining the lattice parameter.

The values of r_A and r_B can be calculated using the equations given below,

$$r_A = \text{Zinc content} \times r_{Zn} + \text{Iron content} \times r_{Fe} \text{ and } r_B = \frac{1}{2}[\text{Nickel content} \times r_{Ni} + \text{Iron content} \times r_{Fe}]$$

The oxygen parameter (u) was calculated using the relation

$$u = [(r_A + R_0)\frac{1}{\sqrt{3}\ a} + \frac{1}{4}] \quad (5)$$

where a is the calculated lattice parameter, R_0 is the radius of oxygen ion (1.38 Å), and r_A is the tetrahedral ionic radius [54]. The calculated values are shown in the Table 4 along with the proposed cation distribution.

The close agreement between the calculated (Table 4) and experimental lattice parameters (Table 1) supports that the proposed distributions are correct. The calculated values of oxygen parameters are very close to that reported value (0.375) in the spinel structure.

Tetrahedral and octahedral bond lengths (d_{AO} and d_{BO}) in a unit cell of spinel lattice have also been estimated using the following relations [55]

$$d_{AO} = a\sqrt{3}(u - 0.25) \quad (6)$$

and

$$d_{BO} = a\left(3u^2 - \frac{11}{4}u + \frac{43}{64}\right)^{\frac{1}{2}} \quad (7)$$

where a is the calculated lattice parameter and u is the calculated oxygen parameter. The observed contraction in Fe^{3+} - O^{2-} bond length at octahedral site in the IE-1000 sample has been reflected in showing the shifting of the octahedral band towards higher frequency and the respective increase in force constant compared with IN-1050 sample.

4. Conclusion

Based on the present study, it is concluded that the sol-gel method proved to be very effective in producing the least sized ferrite particles with reasonably high saturation magnetization. The study establishes that the amount of iron content present in the composition clearly influences the sintering temperature, particle size, specific saturation magnetization, and Curie temperature. Remarkably, a high specific saturation magnetization of 91.9 emu/g has been achieved for the composition containing higher iron content, a desirable value for several biomedical applications. The reduced values of coercivity, Curie temperature and higher saturation magnetization of the investigated materials are very much agreeable with those yielded by the materials useful for biomedical applications.

Acknowledgements

The authors are thankful to the CCMB, Hyderabad for providing TEM facility, Advanced Analytical Laboratory of Andhra University for rendering FTIR facility and SAIF, IIT Madras for providing VSM facility.

References

[1] A. Mahesh Kumar, M. Chaitanya Varma, Charu Lata Dube, K.H. Rao, Subhash C. Kashyap, J. Magn. Magn. Mater. 320 (2008) 1995–2000.
[2] A. Verma, T.C. Goel, R.G. Mendiratta, M.I. Alam, Mater. Sci. Eng. B 60 (1999) 156–162.
[3] M.M. Rashad, E.M. Elsayed, M.M. Moharam, R.M. Abou-Shahba, A.E. Saba, J. Alloys Compd. 486 (2009) 759–767.
[4] M.I. Rosales, E. Amano, M.P. Cuautle, R. Valenzuela, Mater. Sci. Eng. B 49 (1997) 221–226.
[5] S. Zahi, A.R. Daud, M. Hashim, Mater. Chem. Phys. 106 (2007) 452–456.
[6] Su. Hua, Huaiwu Zhang, Xiaoli Tang, Baoyuan Liu, Zhiyong Zhong, J. Alloys Compd 475 (2009) 683–685.
[7] O. Mirzaee, M.A. Golozar, A. Shafyei, Mater. Charact. 59 (2008) 638–641.
[8] Richard Lebourgeois, Sonia Duguey, Jean-Pierre Ganne, J. Magn. Magn. Mater. 312 (2007) 328–330.
[9] Xiang Shen, Yanxin Wang, Xiang Yang, Lu. Liqiang, Liang Huang, J. Mater. Sci: Mater. Electron. 21 (2010) 630–634.
[10] R.C. Kambale, N.R. Adhate, B.K. Chougule, Y.D. Kolekar, J. Alloys Compd. 491 (2010) 372–377.
[11] S. Nasir, A.S. Saleemi, Fatima-tuz-Zahra, M. Anis-ur-Rehman, J. Alloys Compd. 572 (2013) 170–174.
[12] Diandra L. Leslie-Pelecky, Reuben D. Rieke, Chem. Mater. 8 (1996) 1770–1783.
[13] Bashar Issa, Ihab M. Obaidat, Borhan A. Albiss, Yousef Haik, Int. J. Mol. Sci. 14 (2013) 21266–21305.
[14] Hamid Ghayour, Majid Abdellahi, Neriman Ozada, Saeid Jabbrzare, Amirsalar Khandan, J. Phys. Chem. Solids 111 (2017) 464–472.
[15] R. Mondal, S. Dey, S. Majumder, A. Poddar, P. Dasgupta, S. Kumar, J. Magn. Magn. Mater. 448 (2018) 135–145.
[16] Su Hua, Huaiwu Zhang, Xiaoli Tang, Yulan Jing, Yingli Liu, J. Magn. Magn. Mater.

310 (2007) 17–21.
[17] Ling Zhiyuan, Xiong Maoren, Zhang Qingqiu, J. Magn. Magn. Mater. 219 (2000) 9–14.
[18] Ke Sun, Zhongwen Lan, ZhongYu, Xiaona Jiang and JiaominHuang, J. Magn. Magn. Mater. 323 (2011) 927–932.
[19] Xinhua He, Guosheng Song, Jianhong Zhua, Mater. Lett. 59 (2005) 1941–1944.
[20] M. Rahimi, P. Kameli, M. Ranjbar, H. Hajihashemi, H. Salamati, J Mater Sci 48 (2013) 2969–2976.
[21] Mircea Stefanescu, Marcela Stoia, Oana Stefanescu, Paul Barvinschi, J. Therm. Anal. Calorim. 99 (2010) 459–464.
[22] Pengzhao Gao, Xia Hua, Volkan Degirmenci, David Rooney, Majeda Khraisheh, Robert Pollard, Robert M. Bowman, Evgeny V. Rebrov, J. Magn. Magn. Mater. 348 (2013) 44–50.
[23] C. Caizer, M. Stefanescu, Physica B 327 (2003) 129–134.
[24] Elvira Fantechi, Claudia Innocenti, Martin Albino, Elisabetta Lottini, Claudio Sangregorio, J. Magn. Magn. Mater. 380 (2015) 365–371.
[25] M.K. Shobana, Hoon Kwon, Heeman Choe, J. Magn. Magn. Mater. 324 (2012) 2245–2248.
[26] E. Ranjith Kumar, R. Jayaprakash, G. Sarala Devi, P. Siva Prasada Reddy, J. Magn. Magn. Mater. 355 (2014) 87–92.
[27] Lunhong Ai, Jing Jiang, Curr. Appl. Phys. 10 (2010) 284–288.
[28] K. Maaz, Arif Mumtaz, S.K. Hasanain, Abdullah Ceylan, J. Magn. Magn. Mater. 308 (2007) 289–295.
[29] Shifeng Yan, Jingbo Yin, Enle Zhou, J. Alloys Comp. 450 (2008) 417–420.
[30] M. Sertkol, Y. Köseoğlu, A. Baykal, H. Kavas, A.C. Basaran, J. Magn. Magn. Mater. 321 (2009) 157–162.
[31] Zhitao Chen, Lian Gao, Mater. Sci. Eng., B 141 (2007) 82–86.
[32] Zhang Huanque, Hua Fei, Zhang Xuelin, Suo Qiangqiang, Peng Huifen, Wang Xin, J. Magn. Magn. Mater. 439 (2017) 245–250.
[33] Y. Köseoğlu, M. Bay, M. Tan, A. Baykal, H. Sözeri, R. Topkaya, N. Akdoğan, J Nanopart Res 13 (2011) 2235–2244.
[34] Hüseyin Kavas, Abdülhadi Baykal, Muhammet S. Toprak, Yuksel Köseoğlu, Murat Sertkol, Bekir Aktas, J. Alloys Comp. 479 (2009) 49–55.
[35] K. Srinivasa Rao, S.V. Ranga Nayakulu, M. Chaitanya Varma, G.S.V.R.K. Choudary, K.H. Rao, J. Magn. Magn. Mater. 451 (2018) 602–608.
[36] Z.G. Zheng, X.C. Zhong, Y.H. Zhang, H.Y. Yu, D.C. Zeng, J. Alloys Compd 466 (2008) 377–382.
[37] C.H. Chia, S. Zakaria, M. Yusoff, S.C. Goh, C.Y. Haw, Sh. Ahmadi, N.M. Huang, H.N. Lim, Ceram. Int. 36 (2010) 605–609.
[38] D.R.S. Gangaswamy, M. Chaitanya Varma, S. Bharadwaj, K. Sambasiva Rao, K.H. Rao, J. Supercond. Nov. Magn. 28 (2015) 3599–3606.
[39] Ch. Sujatha, K. Venugopal Reddy, K. Sowri Babu, A. Rama Chandra Reddy, K.H. Rao, Ceram. Int. 39 (2013) 3077–3086.
[40] M.M. Mallapur, P.A. Shaikh, R.C. Kambale, H.V. Jamadar, P.U. Mahamuni, B.K. Chougule, J. Alloys Compd. 479 (2009) 797–802.
[41] Montana Sangmanee, Santi Maensiri, Appl. Phys. A 97 (2009) 167–177.
[42] Navneet Singh, Ashish Agarwal, Sujata Sanghi, Paramjeet Singh, Physica B 406 (2011) 687–692.
[43] A. Pradeep, G. Chandrasekaran, Mater. Lett. 60 (2006) 371–374.
[44] P.A. Shaikh, R.C. Kambale, A.V. Rao, Y.D. Kolekar, J. Alloys Compd. 492 (2010) 590–596.
[45] A. Mahesh Kumar, M. Chaitanya Varma, G.S.V.R.K. Choudary, K. Srinivasa Rao, K.H. Rao, G. Gopalakrishna, J. Optoelectron. Adv. M 12 (2010) 2386–2390.
[46] J.S. Ghodake, Rahul C. Kambale, T.J. Shinde, P.K. Maskar, S.S. Suryavanshi, J. Magn. Magn. Mater. 401 (2016) 938–942.
[47] K. Srinivasa Rao, A. Mahesh Kumar, M. Chaitanya Varma, G.S.V.R.K. Choudary, K.H. Rao, J. Alloys Compd. 488 (2009) L6–L9.
[48] N.M. Deraz, J. Anal. Appl. Pyrolysis 88 (2010) 103–109.
[49] A. Mahesh Kumar, Andhra University, Visakhapatnam, Andhra Pradesh, (Ph.D thesis).
[50] Ch. Sujatha, K. Venugopal Reddy, K. Sowri Babu, A. Rama Chandra Reddy, M. Buchi Suresh, K.H. Rao, J. Magn. Magn. Mater. 340 (2013) 38–45.
[51] Jean-Luc Mattei, David Souriou, Alexis Chevalier, J. Magn. Magn. Mater. 447 (2018) 9–14.
[52] B. Parvatheeswara Rao, P.S.V. Subba Rao, G.V.S. Murthy, K.H. Rao, J. Magn. Magn. Mater. 268 (2004) 315–320.
[53] J.S. Ghodake, R.C. Kambale, S.V. Salvi, S.R. Sawant, S.S. Suryavanshi, J. Alloys Comp. 486 (2009) 830–834.
[54] M.A. Gabal, Y.M. AlAngari, J. Magn. Magn. Mater. 322 (2010) 3159–3165.
[55] Santosh Bhukal, Suman Mor, S. Bansal, Jagdish Singh, Sonal Singhal, J. Mol. Struct. 1071 (2014) 95–102.